Is the Aftershock Zone Area a Good Proxy for the Mainshock Rupture Area?

Jing Ci Neo[1], Yihe Huang[1], Dongdong Yao[1], Shengji Wei[2]

[1] University of Michigan, Ann Arbor. 1100 North University, Room 4534F

[2] Asian School of the Environment, Nanyang Technological University. Earth Observatory of Singapore, 50 Nanyang Avenue, Block N2-01a-15

Questions can be directed to neoj@umich.edu

This paper is a non-peer reviewed preprint submitted to EarthArXiv. It has been submitted to Bulletin of Seismological Society America (BSSA) and is currently undergoing peer review.

Abstract Large earthquakes are usually followed by sequences of small earthquakes, exhibiting a mainshock-aftershock pattern. The locations of aftershocks are often observed to be on the same fault plane as the mainshock and used as proxies for its rupture area. However, there has been limited research on how well aftershock location actually approximates mainshock rupture area. Furthermore, recent developments in earthquake relocation techniques have led to great improvements in the accuracy of earthquake locations. Hence, we investigate this assumption using slip distributions and relocated aftershocks of 12 Mw≥5.4 mainshocks in California. We calculate the area enclosed by the aftershocks, normalized by the mainshock rupture area derived from slip contours. We find that overall, the ratios of aftershock zone area to mainshock rupture area, hereinafter referred to as "aftershock ratio", lie within a range of 0.5 to 5.5, with most values larger than 1. Using different slip inversion models for the same earthquake can have a large impact on the results, but the ratios estimated from both the relocated catalogs and Advanced National Seismic System (ANSS) catalog have similar patterns. The ratios for earthquakes in Southern California fall between 0.5 and 3, while earthquakes in Northern California exhibit a wider range of ratios from 1 to 5.5. We also measure aftershock ratios for the early aftershock window (within 1 day) and find a similar range but smaller values than using the entire aftershock duration, suggesting that continuing afterslip could contribute to the expanding aftershock zone area of several mainshocks. Our results show that areas with positive Coulomb stress change scale with aftershock zone areas, indicating that aftershock distribution generally outlines the mainshock rupture area.

1. Introduction

Beginning in the 1930s, scientists believed that aftershock zone area corresponds to the area where strain is accumulated and released during an earthquake sequence (Utsu, 1970). Since then, the aftershock zone area of a mainshock has often been used to approximate its co-seismic rupture area. For example, Kanamori (1977) used the rupture zones defined by the 1-day aftershock zone area to calculate seismic moment and introduce the moment magnitude scale. Kelleher (1972) attempted to forecast potential locations of large South American earthquakes by discerning gaps between their rupture zones, which were defined by the aftershock zone area. Ebel and Chambers (2016) suggested that aftershocks of past major earthquakes can be used to delineate the extent of their ruptures even after decades or centuries. Studies have also found that early aftershocks (within the first 24 hours) tend to occur on the periphery of the aftershock zone, and the aseismic region in the center of the zone corresponds to the extent of the coseismic rupture area (Das and Henry, 2003; Dietz and Ellsworth, 1990).

Different mechanisms have been used to explain various patterns of aftershock occurrence: static stress change, transient dynamic stress change, and postseismic deformation are possible candidates (Freed, 2005). Static stress change is the stress change in the earth's crust surrounding the fault planes due to slip on the faults (King et al., 1994; etc.). In particular, Coulomb stress change became popular in the past few decades with numerous studies attempting to correlate static Coulomb stress change with aftershocks (King et al., 1994; Stein et al., 1997; Hardebeck et al., 1998; Toda et al., 1998; Kilb et al., 2002; Ma et al., 2005; Marsan and Lengliné, 2010; Toda et al., 2011, etc.). Many of the studies found that the distribution of the aftershocks appears to be co-located with regions of positive Coulomb stress change.

However, not all studies agree that static stress change is the only predictor of aftershock distribution, especially the temporal evolution of aftershocks (Cattania et al., 2015). Transient dynamic stress change, which is the stress carried by the passing waves, can trigger "aftershocks" hundreds to thousands of kilometers away and may be related to earthquakes at those locations even months later (Berlardinelli et al, 2003; Parsons, 2014; Fan and Shearer, 2016; van der Elst and Brodsky, 2010). Moreover, by investigating over two hundred slip inversions, Meade et al. (2017) found that other stress change components such as max shear stress and stress invariants, or longer-term changes such as afterslip/postseismic relaxation may be able to account for the spatial distribution of aftershocks better.

Afterslip is the continuing fault slip after the mainshock, and viscoelastic relaxation refers to the release of stress throughout the entire volume of the surrounding viscous lower crust under constant strain (Pollitz et al., 1998; Diao et al., 2013). Both processes have been shown to be able to explain aftershocks distributions. The contribution of each of them is hard to determine, and it depends on the tectonic regime of each earthquake (Perfettini et al 2005). For example, Perfettini and Avouac (2004; 2007) found that the aftershocks of the 1999 Chi-Chi earthquake and the 1992 Landers earthquake correlate well with afterslip in both space and time. Savage et. al. (2007) investigated five large earthquakes and concluded that fault creep alone is not enough to explain the postseismic deformation and aftershocks of those earthquakes; a viscoelastic relaxation term has to be added to the surface deformation equation to obtain a better fit.

However, quantitative models of afterslip and viscoelastic relaxation are less observed and resolved. In this study, we will quantify static Coulomb stress change from mainshock slip and evaluate whether the aftershock zone area could be used as a proxy of the mainshock rupture. Meanwhile, we summarize those published work on afterslip models for some mainshocks and discuss their roles in modulating the aftershock distribution.

The selection of aftershock duration and method to delineate aftershock zone are main factors that affect the calculation of the aftershock zone area. Scientists have previously pointed out that there was no formal agreement on a consistent space-time windowing algorithm to select aftershocks (Knopoff et al., 1982), which is still true to this date. The choice of aftershock duration is tricky as the aftershock zone area could expand with time (Tajima and Kanamori, 1985), and different mechanisms could tangle together with longer durations. Different aftershock durations ranging from one day (Kanamori, 1977), weeks (Wetzler et al, 2018) to years (Parsons, 2002; Perfettini and Avouac, 2007) have been used, depending on the need of each study. Some studies suggested that earthquakes may still have aftershocks decades or centuries later (Bouchon et al., 2013; Ebel and Chambers, 2016). Determining aftershock zone area is difficult too as aftershocks can occur over a large and continuous area especially in places with high background seismicity such as Parkfield, and deciding which earthquakes constitute aftershocks can be quite challenging. Methods used by previous studies include fitting ellipses (Utsu, 1970), drawing energy contours (Tajima and Kanamori, 1985), terminating the aftershock zone based on gaps between the earthquakes (Meng and Peng, 2016), or drawing a simple boundary around the aftershocks (Sykes, 1971). In this study, we use the beta statistic (Matthews and Reasenberg, 1998) to estimate the aftershock duration and aftershock boundary based on the change in seismicity rate after the mainshock since it provides a consistent criterion without empirical assumption.

More recently, developments in seismological techniques have also led to great improvements in the accuracy of earthquake locations and finite fault solutions. This provides an opportunity to reexamine past assumptions using the latest earthquake catalogs and slip models. In this study, we analyze recent moderate to large (Mw≥5.4) earthquakes in California that have relocated earthquake catalogs (Figure 1). We aim to gain insights into earthquake properties and assess the veracity of the assumptions made in the past. Our results can also provide basis for similar assumptions to be made in the future, especially in cases where robust slip inversion is not applicable.

2. Data and Method

We analyze moderate to large (Mw≥5.4) earthquakes in California that have well recorded aftershock sequences as candidate mainshocks (Figure 1). The slip inversion models are obtained from the Finite-Source Rupture Model Database (SRCMOD). On the other hand, we use both relocated catalog (either double-difference or waveform relocated) and Advanced National

Seismic System (ANSS) catalog for following analysis. The relocated catalogs generally have better resolved locations. However, a certain percentage of earthquakes would be dropped during the relocation process and potentially affect the genuine seismicity rate estimation. The ANSS catalog includes all archived earthquakes but endures relatively larger location error. We included both catalogs to evaluate the consistency. More specifically, the double-difference catalogs are acquired from the Northern California Earthquake Data Center (NCEDC) (Waldhauser and Schaff, 2008; Waldhauser, 2009). Waveform relocated catalogs are obtained from the Southern California Earthquake Data Center (SCEDC) (Hauksson et al., 2012). For each mainshock, we download earthquakes that occurred up to 1 year before and after within the surrounding area. The areas used is deliberately much larger than needed to avoid creating an artificial upper limit when calculating the aftershock zone area. A grid of ±1-degree latitude and longitude relative to the mainshock epicenter is used to download earthquakes from NCEDC/SCEDC, while a circle with a radius of five times the source dimension is used to download earthquakes from the ANSS catalog.

Earthquake Selection

To choose earthquakes associated with mainshock faults, only earthquakes with off-fault distances less than 2km to the fault plane from the slip inversion are kept for further analysis. We use 2km because earthquake epicenter location uncertainties typically fall within 2km. We have tried different off-fault distances from 1 to 20km and found that off-fault distances below 5km do not show a large difference. As hypocenter locations given by the slip inversion data and the catalogs are slightly different, we shift the earthquake locations in the catalog using the hypocenter in the slip inversion as a reference for some mainshocks. This ensures that the selection of earthquakes by off-fault distance is accurate and does not affect the calculation of the aftershock zone area. The fault planes are extrapolated past each end, and the earthquakes are then projected onto the nearest fault plane (i.e., smallest fault-normal distance).

Magnitude of Completeness

To remove bias in calculating the change in seismicity rate, we need to ensure that the catalog is complete for both the periods before and after the mainshock, i.e. there are no missing earthquakes for the magnitude range we use. Hence, we calculate the magnitude of completeness (Mc) for both time periods, and only earthquakes with magnitudes above the larger Mc are used. In a few cases, Mc cannot be calculated for either before or after the mainshock, due to the sparsity of data or the shape of the magnitude-frequency distribution (MFD). Hence, we use Mc of the time period that can be calculated instead. The most straightforward way of calculating Mc is the maximum curvature method, which often underestimates Mc for gradually curved bulk MFDs. The Mc95 and Mc90 methods, which calculate the lowest Mc value that gives a best fit of 95% and 90%, provide a closer estimate, but sometimes Mc cannot be calculated when the MFD curve never reaches a 90% fit. Hence, we use the best combination method, whereby an initial estimate is calculated using the max curve, and then the algorithm searches for the Mc95 value and Mc90 value in a fixed range around the estimate. These methods are described in detail in Mignan and Woessner (2012), and we use the open-source MATLAB code written by D. Schorlemmer and J. Woessner (2004) to calculate Mc. We set the magnitude bin size to be 0.1 and do not apply any correction.

Beta Statistic and Aftershock Ratio

We use the β-Statistic to calculate the aftershock zone area. The β-statistic quantifies seismicity rate change based on the difference between the observed and expected number of events occurring in a time period, normalized by the standard deviation of the expected value (Aron and Hardebeck, 2009; Kilb et al., 2000). The standard deviation is calculated by assuming a binomial distribution where earthquakes either occur inside or outside the time period Ta (Matthews and Reasenberg, 1988). A β value of 2, which means 95% significance of increase in seismicity when the β value is normalized by its standard deviation, is used as the threshold to determine if there is a significant increase in seismicity. The equation to calculate the β value is shown below (Equation 1).

$$\beta = \frac{N_a - N * T_a/T}{\sqrt{N(T_a/T)(1 - T_a/T)}} \qquad (1)$$

Where Na is the number of events in the time period of interest, N is the number of events in the entire time period, Ta is the duration of the time period of interest and T is the duration of the entire time period (background window duration Tb plus above defined Ta).

We define the aftershock zone as the region with significant increase in seismicity rate after the mainshock. To find the aftershock zone, we create a grid for the fault plane and the surrounding regions and calculate the β value for each grid cell. A convex boundary is then drawn around those areas with significant change in seismicity using the MATLAB function "boundary" with a 'shrink factor' of 0, which is consistent with results using Delaunay triangulation to denote the boundary. The area enclosed by the boundary is then taken to be the aftershock zone area. Another possible method of calculating the aftershock area is to add up area of cells with significant seismicity rate increase. However, we chose not to use this method mainly because the aftershock zone area increases with cell size, which could be subjective to provide a consistent way to estimate aftershock zone area spanning different magnitudes (Figure S1). In comparison, drawing a boundary around the aftershocks is a robust way to define the aftershock zone area that is largely unaffected by cell size (Table S1). Figure 2 illustrates the calculation of the aftershock zone area. Previous calculations of β values have used different cell sizes such as 2 km (Aron and Hardebeck, 2009) and 6 km (Kilb et al., 2000). As earthquakes are represented as points in the grid, the choice of cell size has an impact on the β values. Using different cell sizes that range from 1 to 4 km, we find that as long as the cell size is large enough such that each earthquake is not isolated, the pattern of β values remains similar. However, a larger cell size like 6 by 6 km (Kilb et al., 2000) is not ideal as it is close to the rupture length of the mainshock, which ranges from 9 to over 100 km in our analysis. Hence, we use a cell size of 2 by 2 km. We locate the areas where the β value is larger than 2 and terminate the aftershock zone area when there is a gap of larger than 15 km (Meng and Peng, 2016). We test a range of gap sizes from 5 to 20 km and find that for small off-fault distances (≤5 km), and the gap size does not affect the results.

The choice of time periods T and Ta can greatly affect the calculation of the aftershock zone area by controlling the number of earthquakes that constitute change in seismicity rate. To estimate the background seismicity rate, we adopt a long-term averaged rate before the mainshock. Previous studies reported obvious increasing foreshocks before some large earthquakes (e.g., Dodge et al., 1995; Hauksson et al., 2002, etc.). However, the short-term foreshock activity should not significantly impact our calculation since we use a much longer window before the mainshock. To test this, we use background window lengths of one year and two years and found that the ratios are generally consistent except for the Whittier Narrows and North Palm Springs earthquake (Figure S2). The range of ratios also remain the same using both pre-shock windows. Since using a pre-shock duration of one year generates more consistent results between the relocated and non-relocated catalogs, we use a pre-shock duration of one year to calculate β values and aftershock zone areas.

Another important parameter is the aftershock duration, which defines the time period when there is still a significantly elevated rate of seismicity in the region. We then calculate the sliding-window β value for the entire faulting system (fault plane and the extended regions) using the aftershocks within an off-fault distance of 2km, with N in equation (1) equal to all the earthquakes that occurred in the region and Ta equal to 10 days after the mainshock. We then slide the time window with a time interval of 5 days and study the evolution of the β value through time. The defined entire aftershock duration is given by the first time-window when the β value drops below the threshold value of 2. The aftershock duration gives Ta, the time period of interest used in the calculation of the β value in each grid cell for each earthquake. The aftershock duration can vary between a few weeks and over a year (Figure 3).

The coseismic rupture area is defined as the area enclosed by a contour of 0.15 of the maximum slip (Wetzler et al., 2018). A slip contour is used because areas with very low slip may not be well resolved and depend greatly on the smoothing method used in the kinematic source inversion. We then calculate the ratio of the aftershock zone area to the coseismic rupture area to investigate how well the aftershock zone area approximates the rupture area. Since each earthquake model is unique, some of them require special processing procedures as listed in Table S2.

Coulomb Stress Change

In order to examine how the mainshock slip impacts the aftershock zone area, we utilize the Coulomb 3 software to calculate the resulting Coulomb stress change of each earthquake (King et al, 1994). We use the entire slip model and the orientation of the main fault plane as the receiver fault to find the Coulomb stress change of the region. Assuming that earthquakes below a certain off-fault distance lie on the same fault plane as the mainshock, we use the orientation of the main fault plane as the receiver fault to find the Coulomb stress change of the region. We also use a friction coefficient of 0.6, although faults have a large range of plausible values between 0 to 0.75 (King et al, 1994). The cross-section of the fault and its surrounding region are calculated with a cell size of 1 by 1 km. We tested thresholds of 0.1 and 1 MPa and find that both will result in a similar trend, but the area enclosed by the 1 MPa cells are more similar to the aftershock zone area observed from the β-Statistic. Hence, we sum the area of the cells that have a positive Coulomb stress change of 1 MPa or more to compare with the aftershock zone area (Figure 4). The results of our Coulomb stress change calculations are listed in Table S3.

3. Results

We analyze a total number of 12 Mw≥5.4 California mainshocks (Table 1), with 3 from the NCEDC double-difference catalog and the rest from the SCEDC waveform relocated catalog. Most of them are strike-slip events, except for the 1994 Northridge earthquake with a thrust mechanism and the 1989 Loma Prieta earthquake with an oblique mechanism. We calculate the ratio of aftershock zone area to mainshock rupture area of each mainshock, often for multiple slip inversion models (Figure 5). The parameters that we used are summarized in Table S4. We also list the data types used by each slip model in Figure 5. Strong ground motion data are predominantly used for Northern California (NC) earthquakes, while various data types are used for Southern California (SC) earthquakes.

We find that aftershock zone areas are within a range of 0.5 to 5.5 times of the mainshock rupture area (Figure 6). Some earthquakes such as the 1989 Loma Prieta earthquake have consistently higher ratios, while others such as the 1999 Hector Mine earthquake and the 1994 Landers earthquake have consistently lower ratios. We explore their potential causes further in the discussion section. Ratios of the same earthquake estimated from different slip inversion models can vary widely. For example, the ratio for the Gallovič (2016) model of the South Napa earthquake is more than 3 times of the ratio for the Wei et al. (2015) model. This is partially because the Wei et al. (2015) model has a peak slip and slip area that is twice as large as the Gallovič (2016) model. The two slip models also assume significantly different fault planes. Since only earthquakes within 2km of the fault planes are included as potential aftershocks, the aftershock zone area estimated for Wei's model is smaller than that for Gallovič's model. Our results also show a similar pattern between the ratios estimated from the ANSS and relocated earthquake catalogs. Table 2 shows that both types of catalogs have almost identical average ratios, but the ANSS catalog has larger variance. We also note that the ratios for Brawley and Elmore Ranch earthquakes differ by a factor of 2 across the relocated and ANSS catalogs. The similar ratios estimated from different catalogs demonstrate that aftershock zone area is a macroscopic source feature that is not sensitive to the differences of earthquake locations in catalogs. We do not observe a clear correlation between moment magnitudes and aftershock ratios either (Figure S3).

Early Aftershock Zone

Above results are based on the entire aftershock duration. Since different aftershock generation mechanisms could affect the long-term aftershock evolution, we also measure ratios using only early aftershocks to exclude postseismic deformation if existed. The early aftershock window is set as 1-day after the mainshock (Kanamori, 1977) and the results are shown in Figure 7. Since the Ta/T term is close to 0 in our study, every single earthquake in each cell after the mainshock would be significant in the output beta value, which could lead to biased results unless an accurate background rate and complete early aftershock catalog are guaranteed. Hence, only the off-fault distance, gap size and Mc are used to determine which aftershocks to include in the analysis. Generally, the ratios for the 1-day duration are smaller than or equal to those for the entire aftershock duration. But the range of median ratios (0.5-3.7) is comparable to the range for the entire aftershock duration (0.5-5.5). The statistics of the early aftershock ratios are shown in Table 2.

4. Discussion

Static Stress Change

If aftershocks are primarily triggered by the Coulomb stress change, they should occur within the area with the positive Coulomb stress change. Hence, we compare the Coulomb stress change area and the aftershock zone area of each mainshock (Figure 3). We find that the Coulomb stress change area shows a positive correlation with the aftershock zone area (Figure 8), which may support the hypothesis of static stress change being a triggering mechanism for aftershocks. However, this correlation does not necessarily mean causation. For example, the correlation may indicate that both static stress changes and aftershock areas are related to certain mainshock source parameters. The correlation between the Coulomb stress change and the aftershock zone area is not an ideal linear trend either, and the discrepancies may be due to the uncertainty of coseismic slip model and the inclusion of other aftershock triggering mechanisms. In particular, the Loma Prieta aftershock zone area appears to be an outlier, as its aftershock zone area is much larger than that of the other earthquakes given its relatively small Coulomb stress change area. We also show the ratio of Coulomb stress area to aftershock area with magnitude (Figure 9), and the results are inconclusive, with either a slight increase or no change in ratio with magnitude depending on the fitting method used.

Afterslip

As Coulomb stress change cannot satisfactorily explain the large aftershock zone area of the Loma Prieta mainshock, an alternative mechanism for aftershock generation is afterslip following the mainshock. The variation of geologic conditions in California results in different amounts of afterslip for each earthquake. The central part of the San Andreas Fault exhibits large amounts of aseismic creep (Khoshmanesh and Shirzaei, 2018), whereas the southern portion is locked with significant slip deficit (Fialko, 2006). Though the underlying reason is not well known, some studies suggest that it might be due to the presence of serpentinite at creeping faults in Northern and Central California (Moore and Rymer, 2007). Studies have shown that the Loma Prieta earthquake has afterslip extending around 40-60km towards the southeast along the San Andreas fault (Behr et al., 1990, Pollitz et al., 1998). The shallow afterslip (above 15km depth) was found to have most likely occurred on the Loma Prieta fault (Bürgmann et al., 1997). Although the afterslip was found to be relatively small (less than 1 cm over 4 months), the afterslip area roughly corresponds to the aftershock zone area in our analysis, which extends southwards for 60 km from the mainshock rupture in a shallow region above 15 km depth. Hence, we argue that the afterslip should account for the large aftershock zone area of Loma Prieta.

Afterslip can occur in the surrounding region loaded by mainshock rupture and transfer stresses on faults that promote the generation of aftershocks. It is unfeasible to quantitatively evaluate the contribution by Coulomb stress change and other mechanisms without detailed rupture simulation based on realistic parameters. For mainshocks with observed afterslip, a combination of the static stress change and afterslip instead of the Coulomb stress change alone could contribute to the positive correlation between the Coulomb stress change area and the aftershock zone area. By comparing the ratios from using both entire aftershock duration (Figure 6) and early aftershocks (Figure 7), we observe that the long-term aftershock duration results in relatively larger ratio for the South Napa, Loma Prieta, Brawley, Joshua Tree and North Palm Springs earthquakes. The larger ratio could be explained by expanding aftershock zones with time caused by postseismic deformation process. In contrast, similar range of aftershock ratios for the other earthquakes support that Coulomb stress change caused by the mainshock rupture plays an important role in aftershock distribution.

We also search for published work on postseismic slip following the studied mainshocks, and seven earthquakes have resolved postseismic slip model (Table S5). For most earthquakes analyzed in the table, the afterslip distribution is similar in extent to our aftershock zone area though their depths may be different, which is consistent with emerging evidences that afterslip could affect the long-term aftershock evolution (Perfettini et al., 2018). To better understand the outlier mainshocks, we could potentially use afterslip models to measure the stress change caused by afterslip, similar to that of Pefettini and Avouac (2004; 2007), to ascertain if it correlates better with their aftershock zone areas. This exceeds the scope of this study and could be a potential work in future with more available afterslip models.

Uncertainty and Limitations

The measurement uncertainties in our calculations include the (1) earthquakes locations, (2) the calculation of Mc, (3) the assumption of threshold β value, (4) the upper limit of the grid and gap size, (5) slip inversion results, and (6) the assumption that the fault plane extends in roughly the same plane outside of the mainshock rupture area. We examine the uncertainty of earthquake locations for the Parkfield mainshock using the Ji (2004) model. We use location uncertainties of 0.5km, 1km and 2km to randomly vary the locations of all the aftershocks. We generate 10,000 synthetic distributions of aftershocks and find the standard deviations of aftershock zone areas are 0.09, 0.12 and 0.15 respectively, which is about 4.8 to 7.8% of the mean value. As the location uncertainties for most earthquakes are smaller than 2km, we believe that the location uncertainty will not greatly affect the ratios.

We calculate Mc before and after the mainshock and remove earthquakes below Mc. Though this procedure ensures that the seismicity change is not biased by the incomplete catalog, it also removes earthquakes from consideration, which may cause the calculated aftershock zone area to be smaller than the real aftershock zone area. To estimate the impact of removing earthquakes below Mc, we calculate the aftershock zone areas of the Brawley and El Mayor-Cucapah mainshocks using the Quake Template Matching (QTM) Catalog for Southern California (Ross et al., 2019) that has a much lower Mc due to the new detections. The ratios of aftershock zone areas to mainshock rupture areas estimated from this catalog are larger than that calculated from the relocated SCEDC catalog (Table S6, Figure S4). However, they are still within the range of ratios (0.5-5) obtained for all the mainshocks.

We limit the calculation of the aftershock zone area by setting a threshold β value of 2. A threshold value of 2 indicates 95% significance of increase in seismicity when we normalize the β value by its standard deviation. The assumption behind the calculation of standard deviation is that each earthquake is an independent event and the probability of an earthquake occurring at any given time is equal. This may not be a valid assumption for earthquakes as the probability of having earthquakes after a mainshock is much higher than before the mainshock, but all metrics for determining aftershock zone area necessarily contain arbitrariness.

We also set an upper limit of the spatial grid and gap to terminate aftershock zone, which may violate the observation of the so-called "global aftershock zone" (Parsons and Geist, 2014; Johnson and Bürgmann, 2016). Among our investigated mainshocks, we noticed an increase of microearthquakes within the Geysers geothermal region following the 2014 Napa earthquake (Figure 2), likely triggered by the passing seismic waves (Meng et al., 2014). More recently, Ross et al. (2019) suggested that the 2010 El Mayor-Cucapah earthquake widely triggered events in Southern California. Hence, we are referring to the traditional aftershock zone in this study, where various triggering mechanisms are comparable.

As shown by the large variations of ratios for different slip models, slip inversion results probably contribute to the largest uncertainty in this study. The estimation of ratios can also be affected by the geometry and orientation of the fault planes as well as the areas enclosed by the slip contours.

Other Results

Studies have shown that aftershocks tend to be concentrated around the boundary of the mainshock rupture zone, with a deficit in the center regions of higher slip (Mendoza and Hartzell, 1988; Dietz and Ellsworth, 1990, Wetzler et al., 2018). This is because most of the strain in the regions of higher slip are already released during the mainshock and hence these areas are less able to generate aftershocks. We test this hypothesis using a slightly modified version of the method used in Wetzler et al 2018. Wetzler et al calculated the distances of aftershocks from the slip contours of several earthquakes, normalized by the radius of a circle that has an area equal to the area enclosed by the slip contour. As many of our slip contours are elongated, we change the normalization constant to the minor axis of an ellipse fitted to the slip contours (Wijewickrema and Papliński, 2004), as shown in Figure 10. The distances are then calculated from the closest slip contour (if there are multiple parts) and normalized by the minor axis of the ellipse fitted to that slip contour. Negative distances refer to distances of aftershocks inside the slip contour while positive distances refer to distances of aftershocks outside the slip contour. We use this method to analyze one slip model from each earthquake (list of models in Table S7). We find that most of the aftershocks are located near the slip contours, within a distance of -0.25 to 0.25 the slip contours. Compared to the results obtained by Wetzler et al. (2018), we find more earthquakes located between 0.5 to 1 distance inside the slip contours (Figure 11), probably because we use the minor axis of an ellipse as the normalization constant. But our results still support the notion that there is a deficit of earthquakes in the central regions of the largest slip.

5. Conclusion

By analyzing 12 mainshocks (Mw≥5.4) in California, we find that the ratios of aftershock zone areas to mainshock rupture areas lie within a range of 0.5 to 5.5, with most values larger than 1. The ratios are smaller for a short aftershock duration of 1 day, ranging from 0.5 to 3.7. Our results suggest that aftershock zone areas can generally be used to approximate mainshock rupture areas for both short and long aftershock durations. Using either the relocated catalog or the ANSS catalog leads to similar patterns of the aftershock zone area. Our results also show that Coulomb stress change exhibit a positive correlation with aftershock zone area. Afterslip distribution is similar in extent to our aftershock zone area for several earthquakes. Therefore, using a combination of different mechanisms may be necessary to fully understand the characteristics of the spatial and temporal distribution of aftershocks.

Data and Resources

Slip inversion data was downloaded from the SRCMOD website at http://equake-rc.info. Earthquake catalogs were obtained from the NCEDC (www.ncedc.org) and SCEDC (http://scedc.caltech.edu) websites and the catalog by Dr. Felix Waldhauser (https://www.ldeo.columbia.edu/~felixw/NCAeqDD/), version NCAeqDD.v201112.1. Coulomb 3 MATLAB codes were downloaded from the USGS website (https://earthquake.usgs.gov/research/software/coulomb/), and open-source MATLAB codes for calculating Mc are written by D. Schorlemmer and J. Woessner (2004). The supplementary material contains additional information about individual earthquakes and results of Coulomb stress change calculations.

Acknowledgements

We thank the CN Yang Scholars Program, Nanyang Technological University, and the University of Michigan for supporting the undergraduate research study of Neo Jing Ci. We would also like to express appreciation to Carissa Tan Xiwen for reviewing this paper.

References

Aron, A., Hardebeck, J. L. (2009). Seismicity Rate Changes along the Central California Coast due to Stress Changes from the 2003 M 6.5 San Simeon and 2004 M 6.0 Parkfield Earthquakes. Bulletin of the Seismological Society of America, Vol. 99, No. 4, 2280-2292, doi: 10.1785/0120080239.

Behr, J., Bilham, R., Bodin, P., Burfoid, R. O., Bürgmann, R. (1990). Aseismic slip on the San Andreas Fault south of Loma Prieta. Geophysical Research Letters, 17, 9, 1445–1448.

Berlardinelli, M. E., Bizzarri, A., Cocco, M. (2003). Earthquake triggering by static and dynamic stress changes. Journal of Geophysical Research, 108, B3, 2135.

Bennett, R. A., Reilinger, R. E., Rodi, W., Li, Y. P., Toksoz, M. N., and Hudnut, K. (1995). Coseismic Fault Slip Associated with the 1992 M(W)-6.1 Joshua-Tree, California, Earthquake - Implications for the Joshua-Tree Landers Earthquake Sequence. Journal of Geophysical Research, 100, B4, 6443-6461

Beroza, G. C. (1991). Near-Source Modeling of the Loma-Prieta Earthquake - Evidence for Heterogeneous Slip and Implications for Earthquake Hazard. Bulletin of the Seismological Society of America, 81, 5, 1603-1621

Bouchon, M., Durand, V., Marsan, D., Karabulut, H., Schmittbuhl, J. (2013). The long precursory phase of most large interplate earthquakes. Nature, 6, 299-302.

Bowman, J. R., Kisslinger, C. (1984). A Test of Foreshock Occurrence in the Central Aleutian Island Arc. Bulletin of the Seismological Society of America, 74, 1, 181-197.

Bürgmann, R., Segall, P., Lisowski, M., Svarc, J. (1997). Postseismic strain following the 1989 Loma Prieta earthquake from GPS and levelling measurements. Journal of Geophysical Research, 102, B3, 4933-4955.

Cattania, C., Hainzl, S., Wang, L., Enescu, B., Roth, F. (2015). Aftershock triggering by postseismic stresses: A study based on Coulomb rate-and-state models. Journal of Geophysical Research, 120, 2388-2407, doi:10.1002/2014JB011500.

Cotton, F., and Campillo. M. (1995). Frequency-Domain Inversion of Strong Motions - Application to the 1992 Landers Earthquake. Journal of Geophysical Research, 100 (B3):3961-3975.

Custodio, S., Liu, P. C., and Archuleta, R. J. (2005). The 2004 Mw 6.0 Parkfield, California, earthquake: Inversion of near-source ground motion using multiple data sets. Geophysical Research Letters, 32 (23).

Das, S. and Henry, C. (2003). Spatial Relation between Main Earthquake Slip and its Aftershock Distribution. Reviews of Geophysics, 41(3), 1013, doi: 10.1029/2002RG000119, 2003.

Diao, F., Xiong, X., Wang, R., Zheng, Y., Walter, T. R., Weng, H., Li, J. (2013). Overlapping post-seismic deformation processes: afterslip and viscoelastic relaxation following the 2011 Mw 9.0 Tohoku (Japan) earthquake. Geophysical Journal International, 196, 1, 218–229, https://doi.org/10.1093/gji/ggt376

Dietz, L. D. and Ellsworth, W. L. (1990). The October 17, 1989, Loma Prieta, California, earthquake and its aftershocks: Geometry of the sequence from high-resolution locations. Geophysical Research Letters, 17, 9, 1417-1420.

Dreger, D. S., Gee, L., Lombard, P., Murray, M. H., and Romanowicz, B. (2005). Rapid finite-source analysis and near-fault strong ground motions: Application to the 2003 M-w 6.5 San Simeon and 2004 Mw 6.0 Parkfield earthquakes. Seismological Research Letters, 76 (1):40-48.

Dodge, D. A., Beroza, G. C., Ellsworth, W. L. (1995). Foreshock sequence of the 1992 Landers, California, earthquake and its implications for earthquake nucleation. Journal of Geophysical Research, 100, B7, 9865-9880.

Ebel, J.E and Chambers, D.W (2016). Using the locations of $M \geq 4$ earthquakes to delineate the extents of the ruptures of past major earthquakes. Geophysical Journal International, 207, 862–875, doi: 10.1093/gji/ggw312.

Emolo, A., and Zollo. A. (2005). Kinematic Source Parameters for the 1989 Loma Prieta Earthquake from the Nonlinear Inversion of Accelerograms. Bulletin of the Seismological Society of America, 95, 3, 981–994.

Fan, W., and Shearer, P. M. (2016). Local near instantaneously dynamically triggered aftershocks of large earthquakes. Science, 353, 6304, 1133-1136.

Fialko, Y. (2006). Interseismic strain accumulation and the earthquake potential on the southern San Andreas fault system. Nature, 441, 968-971, doi:10.1038/nature04797.

Freed, A. M. (2007). Afterslip (and only afterslip) following the 2004 Parkfield, California, earthquake. Geophysical Research Letters, 34, L06312, doi:10.1029/2006GL029155.

Gallovič, F. (2016). Modeling velocity recordings of the Mw6.0 South Napa, California, earthquake: unilateral event with weak high-frequency directivity. Seismological Research Letters, 87, 2-14.

Gulia, L. and Wiemer, S. (2019). Real-time discrimination of earthquake foreshocks and aftershocks. Nature, 574, pp. 193-200.

Hardebeck, J. L., Nazareth, J. J., Hauksson, E. (1998). The static stress change triggering model: Constraints from two southern California aftershock sequence. Journal of Geophysical Research, 103, B10, 24,427-24,437.

Hartzell, S. (1989). Comparison of Seismic Waveform Inversion Results for the Rupture History of a Finite Fault - Application to the 1986 North Palm-Springs, California, Earthquake. Journal of Geophysical Research, 94 (B6):7515-7534.

Hartzell, S. H., and Iida. M. (1990). Source complexity of the 1987 Whittier Narrows, California, earthquake from the inversion of strong motion records. Journal of Geophysical Research, 95 (8):12,475-12,485.

Hauksson, E., Jones, L. M., and Hutton, K. (2002). The 1999 Mw 7.1 Hector Mine, California, Earthquake Sequence: Complex Conjugate Strike-Slip Faulting. Bulletin of Seismological Society of America, 92, 4, 1154-1170.

Hauksson, E., Yang, W., Shearer, P. M. (2012). Waveform Relocated Earthquake Catalog for Southern California (1981 to June 2011). Bulletin of the Seismological Society America, 102, 5, 2239-2244.

Hernandez, B., Cotton, F., and M. Campillo. (1999). Contribution of radar interferometry to a two-step inversion of the kinematic process of the 1992 Landers earthquake. Journal of Geophysical Research,104 (B6):13083-13099.

Ji, C. (2004). Slip history the 2004 (Mw 5.9) Parkfield Earthquake (Single-Plane Model). Retrieved from http://www.tectonics.caltech.edu/slip_history/2004_ca/parkfield2.html, last accessed Mar 26, 2019.

Johnson, C., W., and Bürgmann, R. (2016). Delayed dynamic triggering: Local seismicity leading up to three remote M ≥ 6 aftershocks of the 11 April 2012 M8.6 Indian Ocean earthquake. Journal of Geophysical Research, 121, 134-151, doi:10.1002/2015JB012243.

Jonsson, S., Zebker, H., Segall, P., and Amelung. F. (2002). Fault slip distribution of the 1999 Mw 7.1 Hector Mine, California, earthquake, estimated from satellite radar and GPS measurements. Bull. Seis. Soc. Am 92 (4):1377-1389.

Kanamori, H. (1977). The Energy Release in Great Earthquakes. Journal of Geophysical Research, 82, 20, 2981-2987.

Kaverina, A., Dreger, D., and Price. E. (2002). The combined inversion of seismic and geodetic data for the source process of the 16 October 1999 Mw 7.1 Hector Mine, California, earthquake. Bulletin of the Seismological Society of America, 92 (4):1266-1280.

Kelleher (1972). Rupture Zones of Large South American Earthquakes and Some Predictions. Journal of Geophysical Research, 77, 11, 2087-2103.

Khoshmanesh, M. and Shirzaei, M. (2018). Episodic creep events on the San Andreas Fault caused by pore pressure variations. Nature, Geoscience, volume 11, 610–614.

Kilb, D., Gomberg, J., Bodin, P. (2000). Triggering of earthquake aftershocks by dynamic stresses. Nature, 408, 570-574.

Kilb, D., Gomberg, J., Bodin, P. (2002). Aftershock triggering by complete Coulomb stress changes. Journal of Geophysical Research, 107, B4, ESE 2-1-ESE 2-14.

King, G.C.P, Stein, R.S., Lin, J. (1994). Static Stress Changes and the Triggering of Earthquakes. Bulletin of Seismological Society of America, Vol. 84, No. 3, pp 935-953.

Knopoff, L., Kagan, Y., Knopoff, R. (1982). b Values for Foreshocks and Aftershocks in Real and Simulated Earthquake Sequences. Bulletin of the Seismological Society of America, 72, 5, 1663-1676.

Larsen, S., Reilinger, R., Neugebauer, H., and Strange. W., (1992). Global Positioning System Measurements of Deformations Associated with the 1987 Superstition Hills Earthquake - Evidence for Conjugate Faulting. Journal of Geophysical Research, 97 (B4):4885-4902.

Ma, K. F., Chan, C. H., Stein, R. S. (2005). Response of seismicity to Coulomb stress triggers and shadows of the 1999 Mw = 7.6 Chi-Chi, Taiwan, earthquake. Journal of Geophysical Research, 110, B05S19, doi:10.1029/2004JB003389.

Marsan, D. and Lengliné, O. (2010). A new estimation of the decay of aftershock density with distance to the mainshock. Journal of Geophysical Research, 115, B09302.

Matthews, M. V., Reasenberg, P. A. (1988). Statistical Methods for Investigating Quiescence and Other Temporal Seismicity Patterns. Pure and Applied Geophysics, 126, 2-4, 357-372.

Meade, B. J., DeVries, P. M. R., Faller, J., Viegas, F., & Wattenberg, M. (2017). What is better than Coulomb failure stress? A ranking of scalar static stress triggering mechanisms from 10 mainshock-aftershock pairs. Geophysical Research Letters, 44, 11,409–11,416, doi: https://doi.org/10.1002/2017GL075875.

Mendoza, C., and Hartzell. S. H., (1988). Inversion for slip distribution using teleseismic P waveforms; North Palm Springs, Borah Peak, and Michoacan earthquakes. Bulletin of the Seismological Society of America, 78 (3):1092-1111.

Mendoza, C. and Hartzell, S. (2013). Finite-fault source inversion using teleseismic P waves: Simple parameterization and rapid analysis. Bulletin of the Seismological Society of America, 103(2A), 834-844.

Meng, X., Peng, Z. (2016). Increasing lengths of aftershock zones with depths of moderate-size earthquakes on the San Jacinto Fault suggests triggering of deep creep in the middle crust. Geophysical Journal International, 204, 250-261, doi: 10.1093/gji/ggv445.

Meng, X., Peng, Z., Aiken, C., Kilb, D. (2014). Dynamically triggered earthquakes in the Geysers region following the 2014 M6.0 South Napa earthquake, Eos AGU Fall Meeting.

Mignan, A., J. Woessner (2012), Estimating the magnitude of completeness in earthquake catalogs, Community Online Resource for Statistical Seismicity Analysis, doi:10.5078/corssa-00180805. Available at http://www.corssa.org.

Moore, D. E., Rymer, M. J. (2007). Talc-bearing serpentinite and the creeping section of San Andreas Fault. Nature, 448, 795-797.

NCEDC (2014), Northern California Earthquake Data Center. UC Berkeley Seismological Laboratory. Dataset. doi:10.7932/NCEDC.

Parsons, T. (2002). Global Omori law decay of triggered earthquakes: Large aftershocks outside the classical aftershock zone. Journal of Geophysical Research, 107, B9, 2199, doi: 10.1029/2001JB000646.

Parsons, T., Geist, E. L. (2014). The 2010–2014.3 global earthquake rate increase. Geophysical Research Letters, 41, 13, 4479-4485.
Perfettini, H., Avouac, J. P. (2007). Modeling afterslip and aftershocks following the 1992 Landers earthquake. Journal of Geophysical Research, 112, B07409, doi:10.1029/2006JB004399.
Perfettini, H., Avouac, J. P., Ruegg, J. C. (2005). Geodetic displacements and aftershocks following the 2001 Mw = 8.4 Peru earthquake: Implications for the mechanics of the earthquake cycle along subduction zones. Journal of Geophysical Research, 110, B09404, doi:10.1029/2004JB003522
Pollitz, F. F., Bürgmann, R., Segall, P. (1998). Joint estimation of afterslip rate and postseismic relaxation following the 1989 Loma Prieta earthquake. Journal of Geophysical Research, 103, B11, 26,975-26,992.
Ross, Z.E., Trugman, D.T., Hauksson, E., and P.M. Shearer (2019). Searching for Hidden Earthquakes in Southern California. Science, 364, 6442, 767-771.
Savage, J. C., Svarc, J. L., Yu, S. B. (2007). Postseismic relaxation and aftershocks. Journal of Geophysical Research, 112, B06406, doi: 10.1029/2006JB004584.
SCEDC (2013): Southern California Earthquake Center. Caltech Dataset. doi:10.7909/C3WD3xH1.
Sykes, L. R. (1971). Aftershock Zones of Great Earthquakes, Seismicity Gaps, and Earthquake Prediction for Alaska and the Aleutians. Journal of Geophysical Research, 76(32), 8021-8041.
Tajima, F., Kanamori, H. (1985). Global survey of aftershock zone area expansion patterns. Physics of the Earth and Planetary Interiors, 40, 77-134.
Toda, S., Stein, R. S., Reasenberg, P. A., Dieterich, J. H., Yoshida, A. (1998). Stress transferred by the 1995 Mw -- 6.9 Kobe, Japan, shock: Effect on aftershocks and future earthquake probabilities. Journal of Geophysical Research, 103, B10, 24 543-24565.
Toda, S., Stein, R. S., Lin, J. (2011). Widespread seismicity excitation throughout central Japan following the 2011 M=9.0 Tohoku earthquake and its interpretation by Coulomb stress transfer. Geophysical Research Letters, 38, L00G03, doi:10.1029/2011GL047834.
USGS (2019). ANSS Comprehensive Earthquake Catalog (ComCat). Retrieved from https://earthquake.usgs.gov/earthquakes/search/
Utsu, T. (1970). Aftershocks and Earthquake Statistics (1): Some Parameters Which Characterize an Aftershock Sequence and Their Interrelations. Journal of the Faculty of Science, Hokkaido University. Series 7, Geophysics, 3(3): 129-195.
Van der Elst, N. J., and Brodsky, E. E. (2010). Connecting near-field and far-field earthquake triggering to dynamic strain. Journal of Geophysical Research, 115, B07311.
Wald, D. J., T. H. Heaton, and K. W. Hudnut. 1996. The slip history of the 1994 Northridge, California, earthquake determined from strong-motion, teleseismic, GPS, and leveling data. Bulletin of the Seismological Society of America, 86 (1): S49-S70.
Wald, D. J., Helmberger, D. V., and Heaton. T. H. (1991). Rupture Model of the 1989 Loma-Prieta Earthquake from the Inversion of Strong-Motion and Broad-Band Teleseismic Data. Bulletin of the Seismological Society of America, 81 (5):1540-1572.
Waldhauser, F., Near-real-time double-difference event location using long-term seismic archives, with application to Northern California, Bulletin of the Seismological Society of America, 99, 2736-2848, doi:10.1785/0120080294, 2009.
Waldhauser, F. and D.P. Schaff (2008). Large-scale relocation of two decades of Northern California seismicity using cross-correlation and double-difference methods, J. Geophys. Res., 113, B08311, doi:10.1029/2007JB005479.
Wei, S., Fielding, E., Leprince, S., Sladen, A., Avouac, J.P., Helmberger, D., Hauksson, E., Chu, R., Simons, M., Hudnut, K., Herring T., and Briggs, R. (2011). Superficial simplicity of the 2010 El Mayor-Cucapah earthquake of Baja California in Mexico. Nature Geoscience. doi:10.1038/ngeo1213.
Wei, S., Helmberger, D. V., Owen, S., Graves, R. W., Hudnut, K. W., and Fielding, E. (2013). Complementary slip distributions of the largest earthquakes in the 2012 Brawley swarm, Imperial Valley, California. Geophysical Research Letters, 40, 1-6, doi:10.1002/grl.50259.
Wei, S., Barbot, S., Graves, R., Lienkaemper, J. J., Wang, T., Hudnut, K., Fu, Y., and Helmberger, D. (2015). The 2014 Mw 6.1 South Napa Earthquake: A Unilateral Rupture with Shallow Asperity and Rapid Afterslip. Seismological Research Letters, 86(2A), 344-354.
Wells, D. L., Coppersmith, K. J. (1994). New Empirical Relationships among Magnitude, Rupture Length, Rupture Width, Rupture Area, and Surface Displacement. Bulletin of the Seismological Society of America, Vol. 84, No. 4., pp 974 – 1002.

Wetzler, N., Lay, T., Brodsky, E., Kanamori, H., (2018). Systematic deficiency of aftershocks in areas of high coseismic slip for large subduction zone earthquakes. Science Advances, 4(2) eaao3225, DOI: 10.1126/sciadv.aao3225.
Wijewickrema, S. N. R., Paplinski, A. P. (2004). Principal Component Analysis for the Approximation of a Fruit as an Ellipse.
Zeng, Y., and Anderson. J. (2000). Evaluation of numerical procedures for simulating near-fault long-period ground motions using Zeng method. Report 2000/01 to the PEER Utilities Program, available at http://peer.berkeley.edu

Full Mailing Addresses of Authors

Jing Ci Neo
University of Michigan, Ann Arbor. Room 4534F, 1100 North University

Yihe Huang
University of Michigan, Ann Arbor. Room 4534F, 1100 North University

Dongdong Yao
University of Michigan, Ann Arbor. Room 4534F, 1100 North University

Shengji Wei
Earth Observatory of Singapore, 50 Nanyang Avenue, Block N2-01a-15

List of Tables

Table 1
Summary of the source properties and ratios of earthquakes.

Earthquake	Date	Location N/W	Magnitude (Mw)	Depth (km)	Slip Inversion References	Data Sources*	Reloc.	ANSS
South Napa (SN)	2014/08/24	38.22/122.31	6.10	11.0	Wei et al (2015)	SGM	1.04	0.92
			6.07	10.0	Gallovič (2016)	SGM	4.16	3.66
Parkfield (Pf)	2004/09/28	35.82/120.37	5.90	8.0	Ji (2004)	SGM, GPS	1.28	2.04
			6.00	8.3	Dreger et al (2005)	SGM, GPS	2.37	2.70
			6.06	8.3	Custodio et al (2005)	SGM	2.36	2.18
Loma Prieta (LP)	1989/10/18	37.04/121.88	6.98	17.6	Zeng and Anderson (2000)	SGM	5.38	4.54
			6.94	17.6	Wald et al (1991)	SGM, TELE	4.19	3.53
			6.96	17.6	Beroza (1991)	SGM	3.82	5.23
			6.91	17.6	Emolo and Zollo (2005)	SGM	3.40	4.69
Brawley Swarm (BS)	2012/08/26	33.02/115.54	5.45	6.4	Wei et al (2013)	SGM, GPS	0.82	2.29
El-Mayor-Cucapah (EMC)	2010/04/04	32.30/115.30	7.35	10.0	Mendoza and Hartzell (2013)	TELE	2.17	2.61
			7.29	5.5	Wei et al (2011)	TELE, SPOT, GPS, INSAR, SAR	1.79	1.74
Hector Mine (HM)	1999/10/16	34.59/116.27	7.24	6.0	Kaverina et al (2002)	SGM, GPS	1.26	1.18
			7.16	15.0	Jonsson et al (2002)	GPS, INSAR	1.49	0.98
Northridge (Nr)	1994/01/17	34.21/118.54	6.71	17.5	Zeng and Anderson (2000)	SGM	2.33	3.01
			6.80	17.5	Wald et al (1996)	SGM, TELE, GPS	1.30	1.88
			6.81	17.5	Hudnut et al (1996)	TRIL, GPS	1.38	1.67
			6.73	17.5	Hartzell et al (1996)	SGM	1.21	1.49
Landers (Ld)	1992/06/28	34.20/116.43	7.20	7.0	Zeng and Anderson (2000)	SGM	1.15	0.88
			7.22	7.0	Hernandez et al (1999)	SGM, GPS	1.80	1.26
			7.29	7.0	Cotton and Campillo (1995)	SGM	1.47	1.15
Joshua Tree (JT)	1992/04/23	34.00/116.32	6.25	12.5	Bennett et al (1995)	TRIL, GPS	2.12	1.96
Elmore Ranch (ER)	1987/11/24	33.08/115.80	6.52	10.0	Larsen et al (1992)	TRIL, GPS	4.30	2.06
Whittier Narrows (WN)	1987/10/01	34.05/118.08	5.89	14.6	Hartzell and Iida (1990)	SGM	1.61	NA
North Palm Springs (NPS)	1986/07/08	34.00/116.57	6.14	11.0	Hartzell (1989)	SGM	0.54	0.79
			6.21	11.0	Mendoza and Hartzell (1988)	TELE	1.87	2.72

*SGM: Strong ground motion, TELE: Teleseismic data, GPS: Global Positioning System, SAR: Synthetic-Aperture Radar, INSAR: Interferometric Synthetic-Aperture Radar, SPOT: Optical imaging from the SPOT-5 satellite.

Table 2
Statistics of the ratios

	Entire Duration		1-Day Aftershocks	
	Relocated Catalogs	ANSS Catalog	Relocated Catalogs	ANSS Catalog
Mean	2.18	2.16	1.79	1.79
Variance	1.58	1.90	0.64	1.28
Median	1.80	2.00	1.67	1.73
Mean Absolute Deviation	0.98	1.03	0.67	0.94

List of Figure Captions

Figure 1. Map of mainshock locations in this study. Known faults are specified as dark red lines, and the direction of plate motion is indicated by black arrows.

Figure 2. Illustration of how the aftershock zone area of each mainshock is defined using the β values. The diagrams show the fault plane view, with β values of each grid cell calculated from the aftershocks projected on to the fault plane. Aftershocks from the relocated catalogs are used for this figure.

Figure 3. Illustration of how aftershock duration is calculated. The horizontal black line is at a β value of 2, and the aftershock duration is taken to be the end of the time window where the β value first dips below the line (indicated by the stars). If the β value never dips below 2, 1 year is used. For example, the aftershock durations for Parkfield and Northridge are the same (>1 year).

Figure 4. Depiction of how the coulomb stress change area is calculated. For illustration, a contour is drawn around the boundary of cells with a positive coulomb stress change of >1 MPa or more. The coulomb stress change area is given by the sum of the area of these cells.

Figure 5. Plot of the data types used for each slip inversion, where the ratios are calculated using the relocated catalogs. SGM: Strong ground motion; Teleseismic: Teleseismic waveform data; Geodetic: GPS, INSAR.

Figure 6. Plot of ratios sorted by earthquake, with the full names of each earthquake in Table 1. The black crosses represent ratios of different slip inversion models for each earthquake, while the red dots represent the median values of the ratios. (Left) NCEDC data is used to calculate the aftershock zone area for the first 3 earthquakes, while SCEDC data is used for the rest of the earthquakes. (Right) ANSS catalog is used. The ratio for the Whittier Narrows (WN) earthquake is not obtained from the ANSS catalog because the data does not yield a robust estimation of the magnitude of completeness.

Figure 7. Aftershock ratios calculated from 1-day aftershock durations for both earthquake catalogs.

Figure 8. Aftershock zone area vs. Coulomb stress change area.

Figure 9. Robust fitting (solid line) and least squares fitting (dashed line) of ratios of Coulomb stress area to aftershock zone area with magnitude.

Figure 10. Illustration of how the distances from slip contour are calculated using the Parkfield, Chen Ji et al slip model.

Figure 11. Histogram of aftershock distances from slip contours for all earthquakes using the relocated and ANSS catalogs.

List of Figures

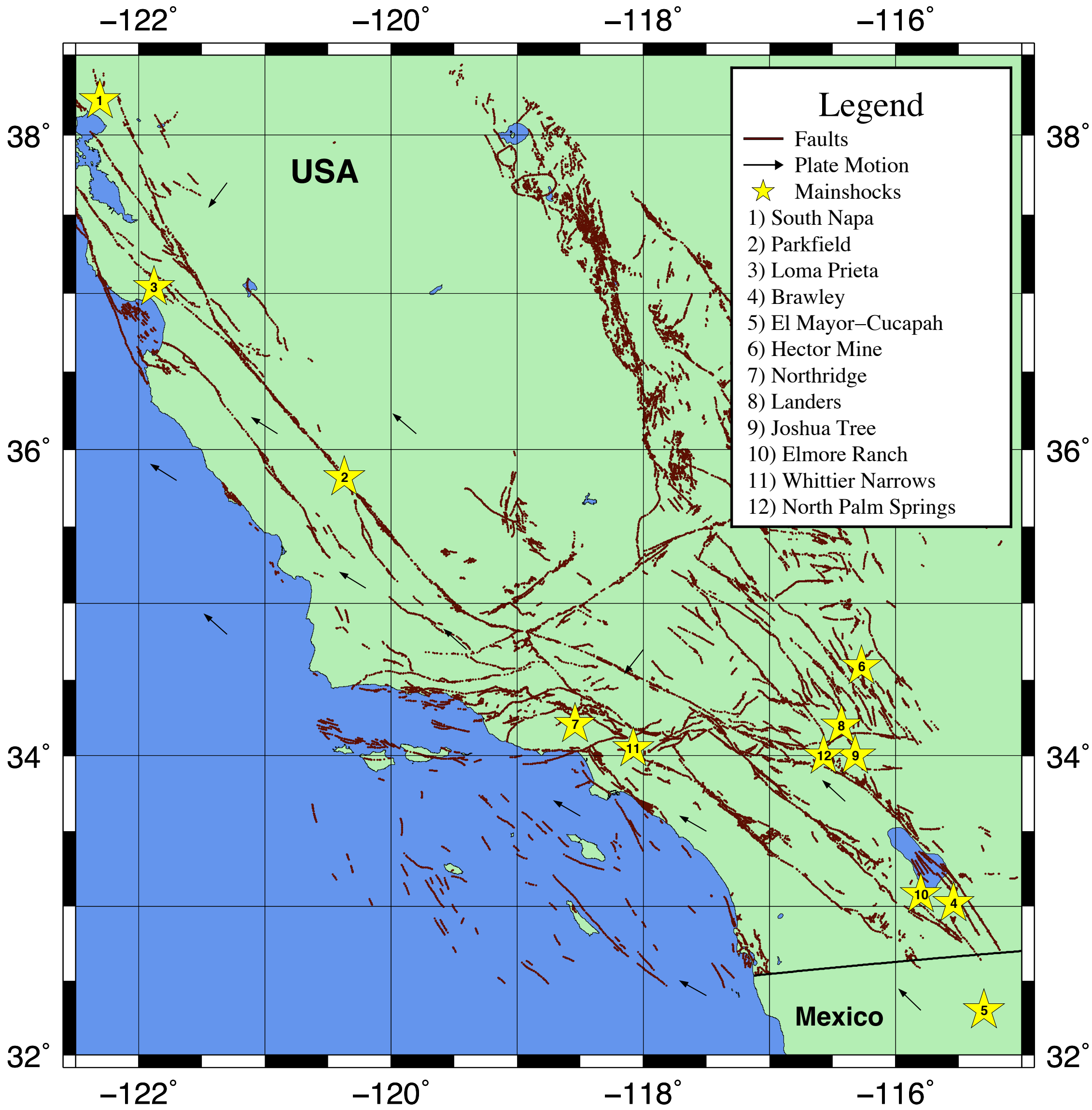

Figure 1. Map of mainshock locations in this study. Known faults are specified as dark red lines, and the direction of plate motion is indicated by black arrows.

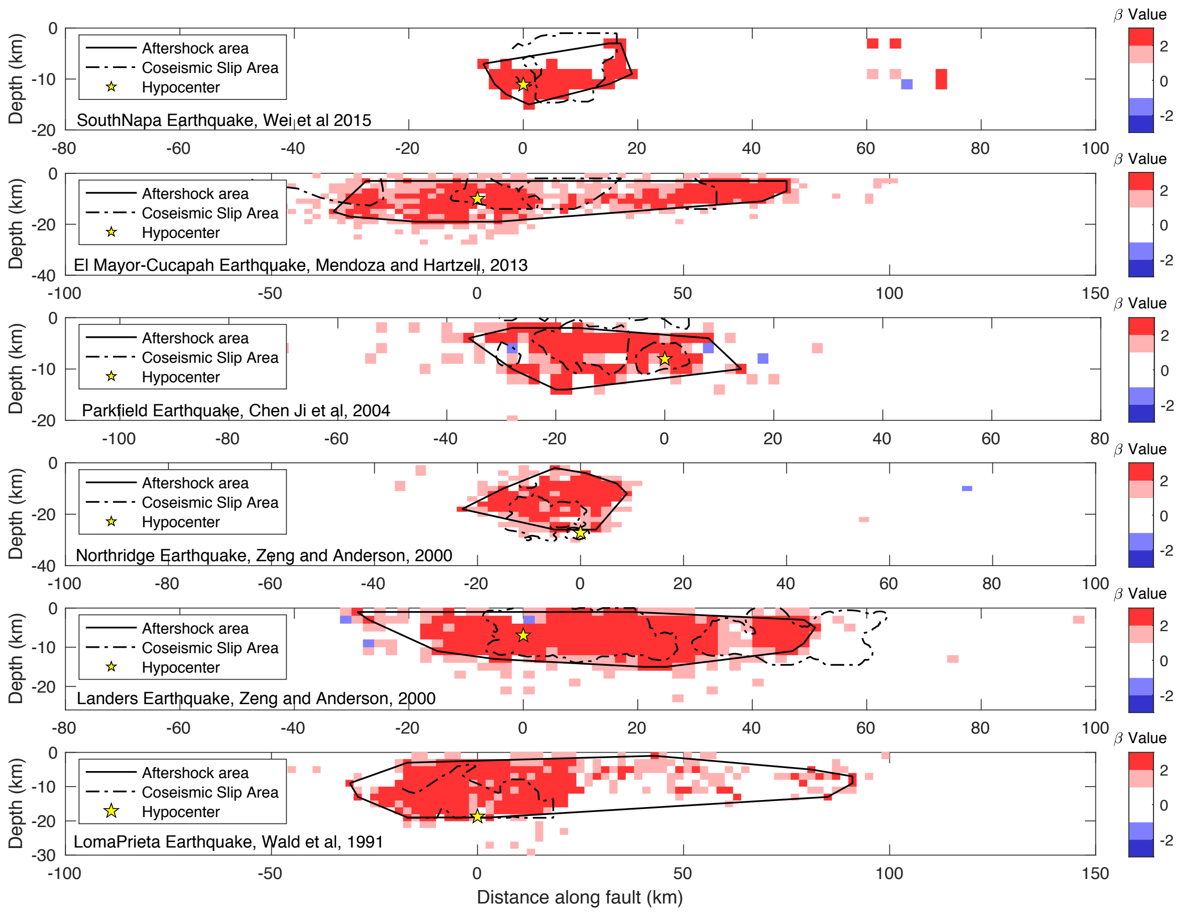

Figure 2. Illustration of how the aftershock zone area of each mainshock is defined using the β values. The diagrams show the fault plane view, with β values of each grid cell calculated from the aftershocks projected on to the fault plane. Aftershocks from the relocated catalogs are used for this figure.

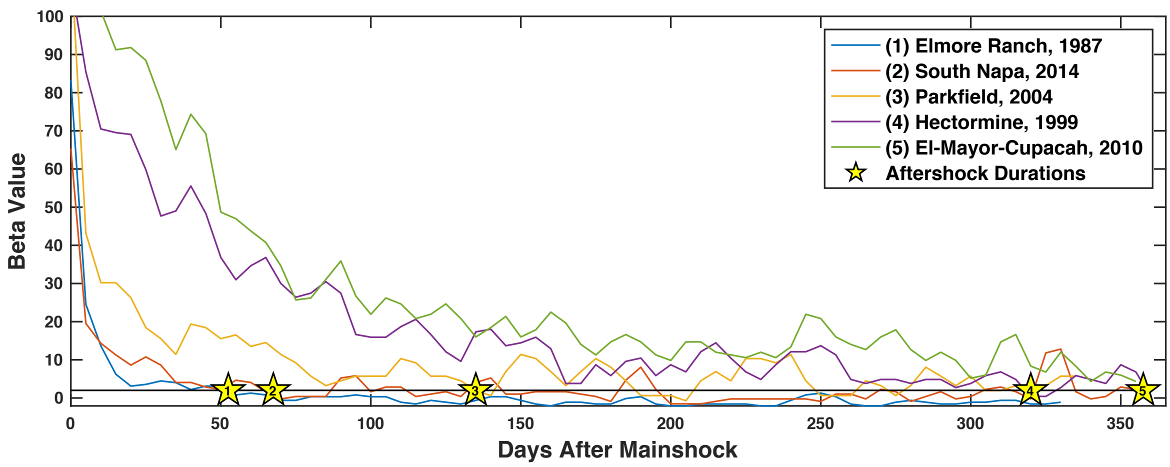

Figure 3. Illustration of how aftershock duration is calculated. The horizontal black line is at a β value of 2, and the aftershock duration is taken to be the end of the time window where the β value first dips below the line (indicated by the numbered stars). If the β value never dips below 2, 1 year is used.

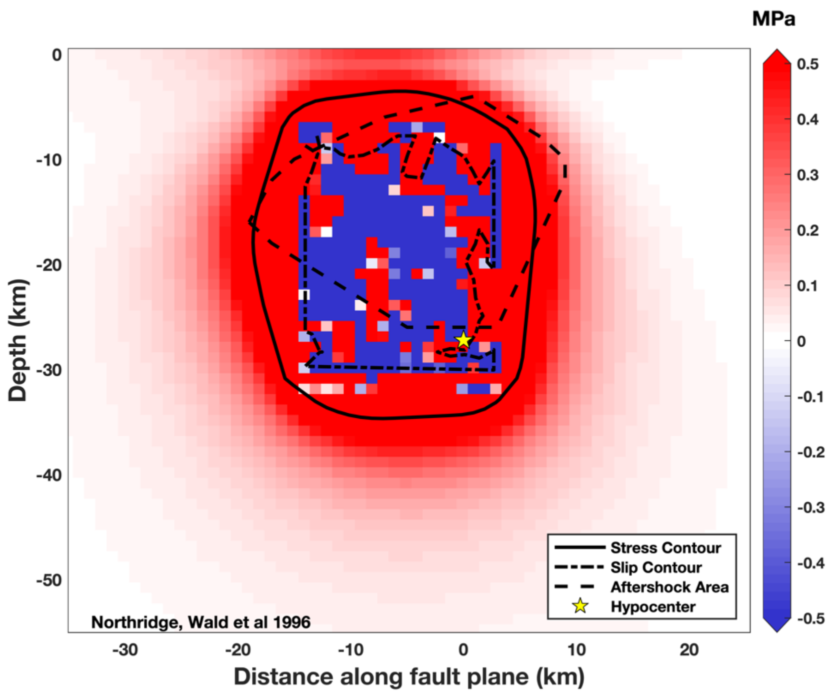

Figure 4. Depiction of how the coulomb stress change area is calculated. For illustration, a contour is drawn around the boundary of cells with a positive coulomb stress change of >1 MPa or more. The coulomb stress change area is given by the sum of the area of these cells.

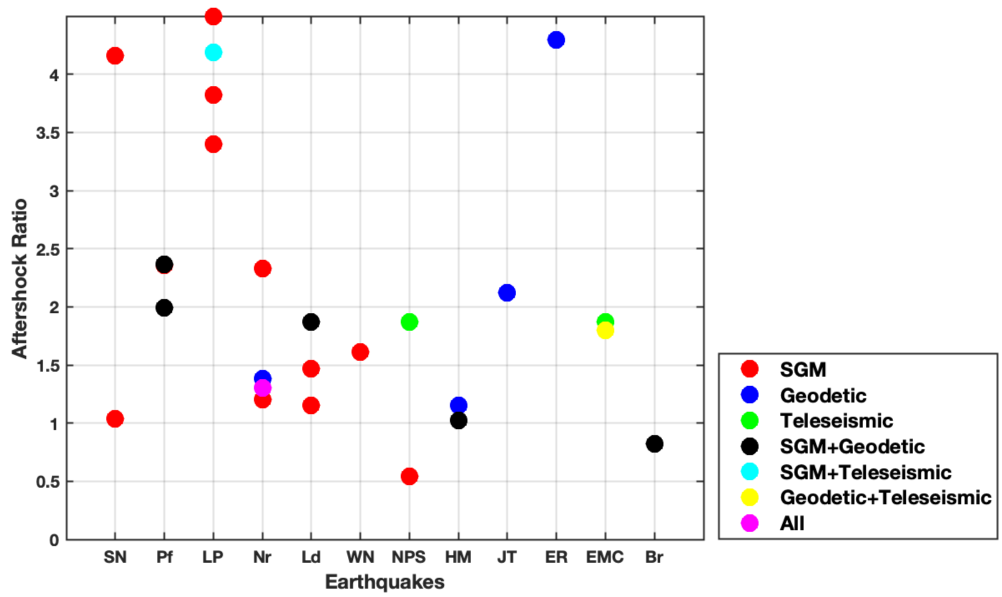

Figure 5. Plot of the data types used for each slip inversion, where the ratios are calculated using the relocated catalogs. SGM: Strong ground motion; Teleseismic: Teleseismic waveform data; Geodetic: GPS, INSAR.

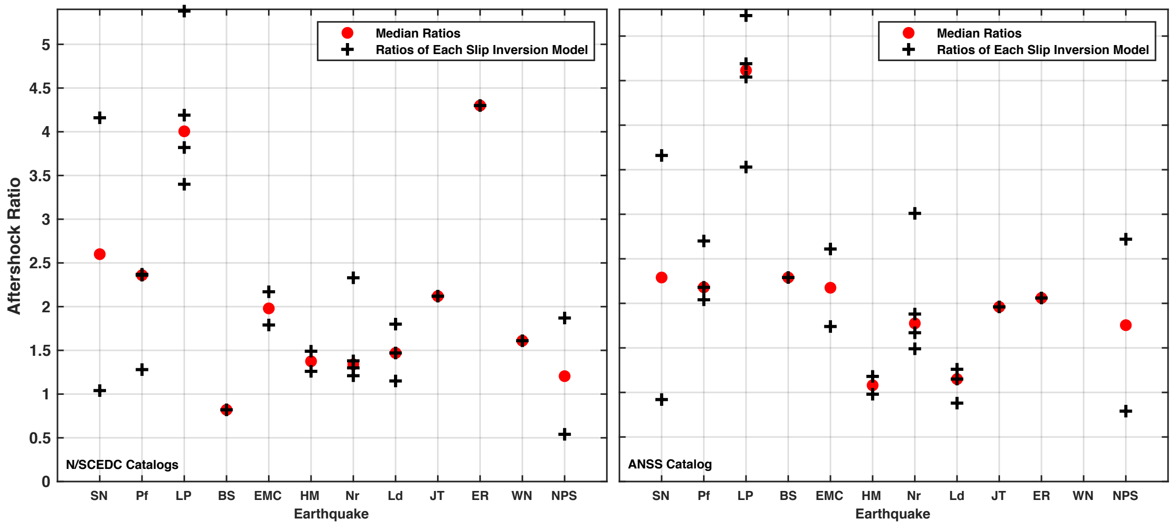

Figure 6. Aftershock zone area ratios for different earthquakes using different earthquake catalogs, with the full names of each earthquake in Table 1. The black crosses represent ratios of different slip inversion models for each earthquake, while the red dots represent the median values of the ratios. (Left) NCEDC data is used to calculate the aftershock zone area for the first 3 earthquakes, while SCEDC data is used for the rest of the earthquakes. (Right) ANSS catalog is used. The ratio for the Whittier Narrows (WN) earthquake is not obtained from the ANSS catalog because the data does not yield a robust estimation of the magnitude of completeness.

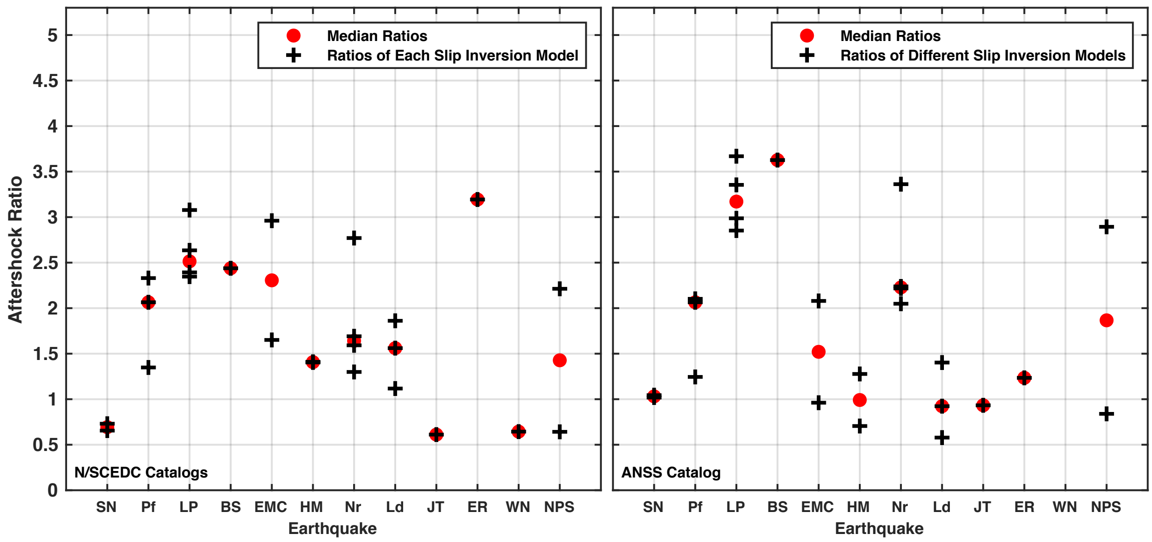

Figure 7. Aftershock ratios calculated from 1-day aftershock durations for both earthquake catalogs.

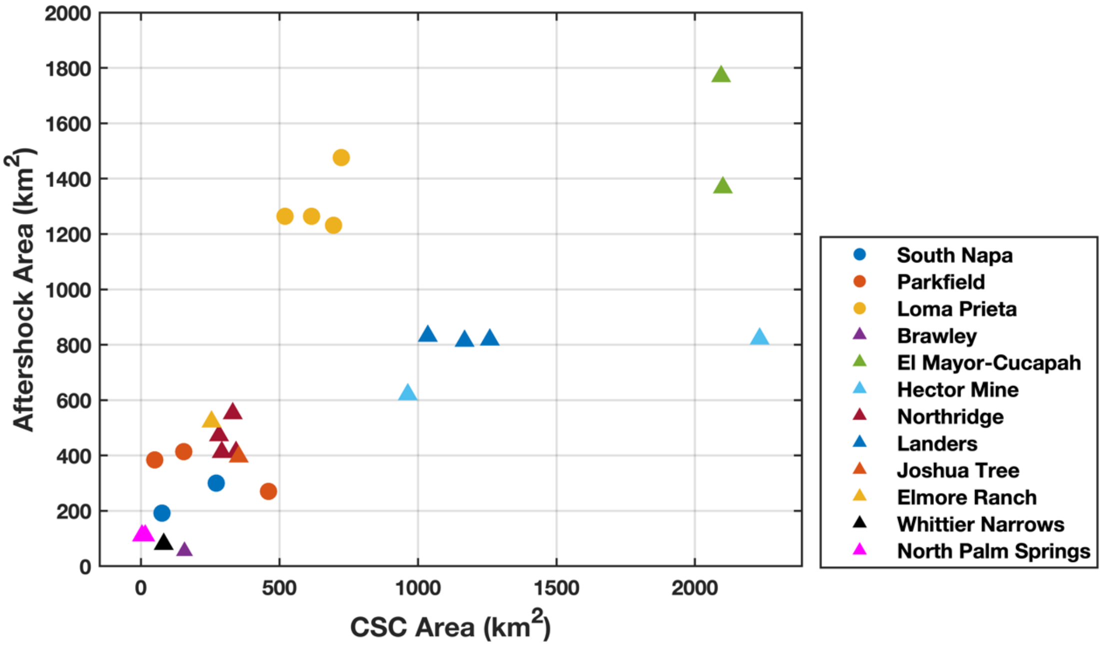

Figure 8. Aftershock zone area vs. Coulomb stress change area.

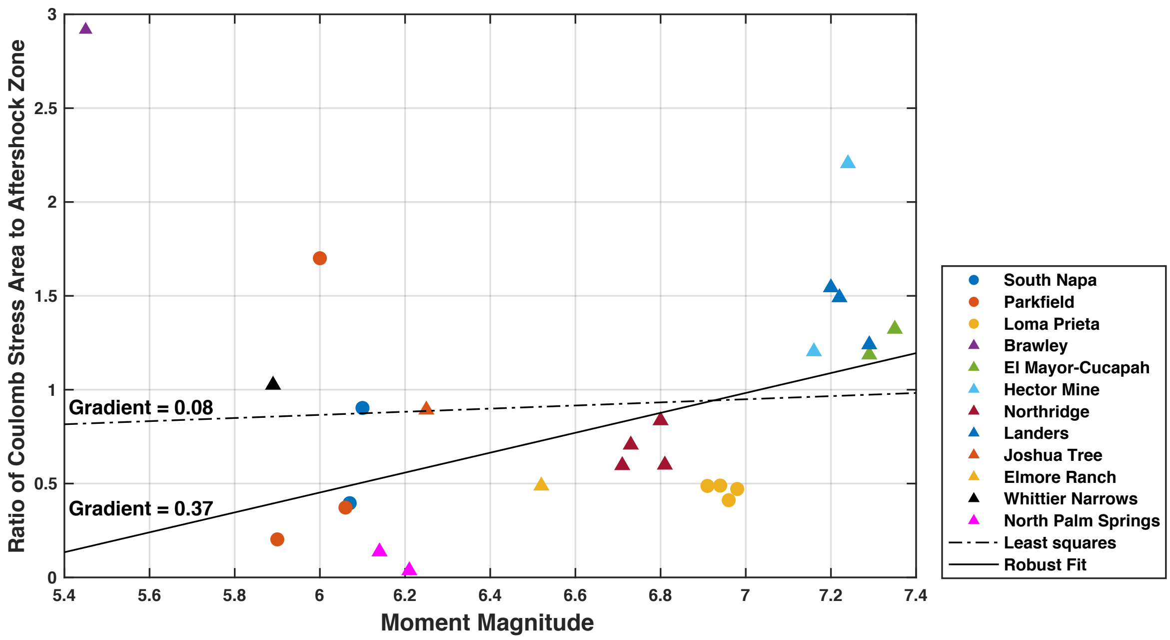

Figure 9. Robust fitting (solid line) and least squares fitting (dashed line) of ratios of Coulomb stress area to aftershock zone area with magnitude.

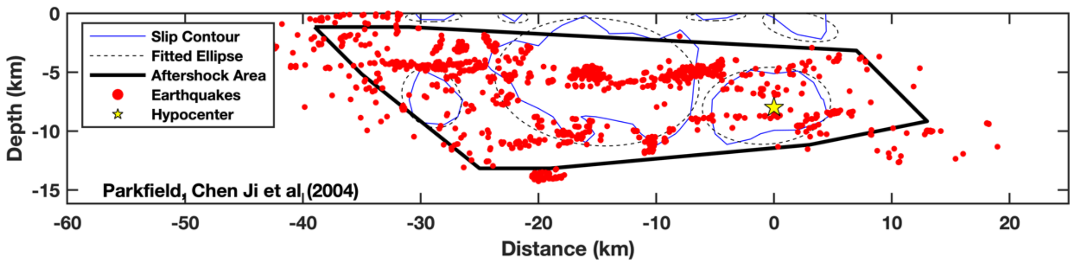

Figure 10. Illustration of how the distances from slip contour are calculated using the Parkfield, Chen Ji et al slip model.

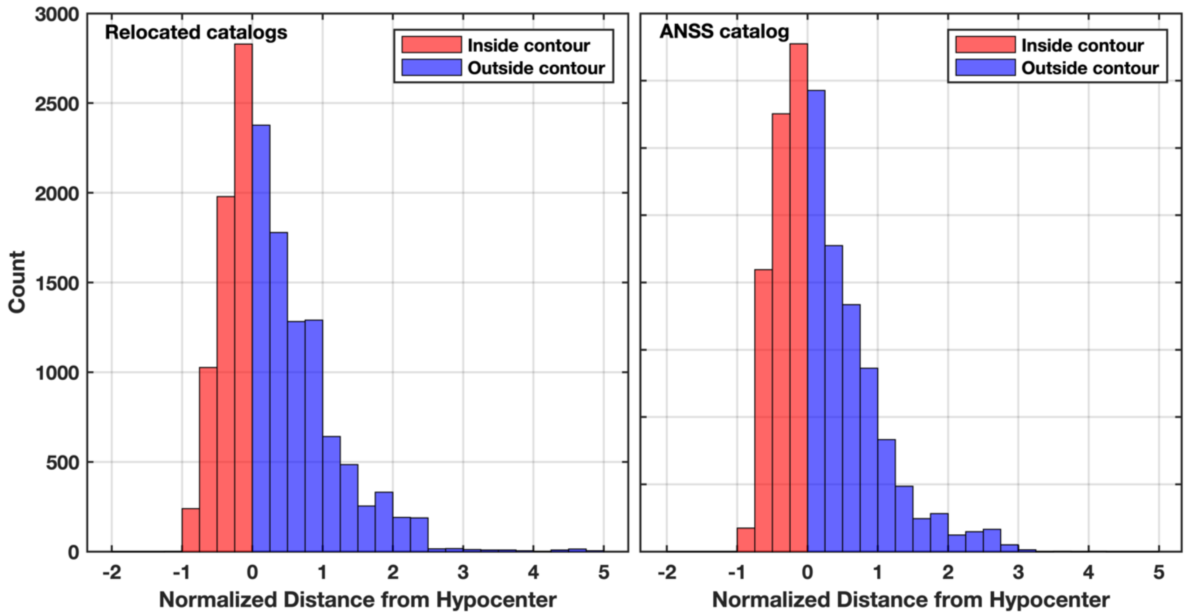

Figure 11. Histogram of aftershock distances from slip contours for all earthquakes using the relocated and ANSS catalogs.